

# Comprehensive *ab initio* study of effects of alloying elements on generalized stacking fault energies of Ni and Ni<sub>3</sub>Al

Heyu Zhu,<sup>1,2</sup> Jiantao Wang,<sup>1,2</sup> Yun Chen,<sup>1</sup> Mingfeng Liu,<sup>1,2</sup> Hui Ma,<sup>1</sup> Yan Sun,<sup>1</sup> Peitao Liu,<sup>1,\*</sup> and Xing-Qiu Chen<sup>1,†</sup>

<sup>1</sup>Shenyang National Laboratory for Materials Science, Institute of Metal Research,  
Chinese Academy of Sciences, 110016 Shenyang, China.

<sup>2</sup>School of Materials Science and Engineering, University of Science and Technology of China, 110016 Shenyang, China.

Excellent high-temperature mechanical properties of Ni-based single crystal superalloys (NSCSs) are attributed to the yield strength anomaly of Ni<sub>3</sub>Al that is intimately related to generalized stacking fault energies (GSFEs). Therefore, clarifying the effects of alloying elements on the GSFEs is of great significance for alloys design. Here, by means of *ab initio* density functional theory calculations, we systematically calculated the GSFEs of different slip systems of Ni and Ni<sub>3</sub>Al without and with alloying elements using the alias shear method. We obtained that for Ni, except for magnetic elements Mn, Fe, and Co, most of alloying elements decrease the unstable stacking fault energy ( $\gamma_{usf}$ ) of the  $[01\bar{1}](111)$  and  $[11\bar{2}](111)$  slip systems and also decrease the stable stacking fault energy ( $\gamma_{sf}$ ) of the  $[11\bar{2}](111)$  slip system. Interestingly, the reduction effects exhibit a strong correlation with the inverse of atom radii. For Ni<sub>3</sub>Al, most of alloying elements in groups IIIB-VIIB show a strong Al site preference. Except for Mn and Fe, the elements in groups VB-VIIB and the first column of group VIII increase the values of  $\gamma_{usf}$  of different slip systems of Ni<sub>3</sub>Al, which makes the slip deformation and dislocation emits difficult. On the other hand, the elements in groups IIIB-VIIB also increase the value of  $\gamma_{sf}$ , and thus reduce the stability of the antiphase boundary, complex stacking fault and superlattice intrinsic stacking fault of Ni<sub>3</sub>Al. We found that Re is an excellent strengthening alloying element that significantly increases the slip barrier of the trailing slip process for Ni, and also enhances the slip barrier of the leading slip process of three slip systems for Ni<sub>3</sub>Al. W and Mo exhibit similar effects as Re. We predicted that Os, Ru, and Ir are good strengthening alloying elements as well, since they show the strengthening effects on both the leading and trailing slip process for Ni and Ni<sub>3</sub>Al. This work established an exhaustive dictionary of the effects of various alloying elements on the GSFEs of both Ni and Ni<sub>3</sub>Al phases, which would aid to guide the design of next-generation high-performance NSCSs.

## I. INTRODUCTION

Nickel-based single crystal superalloys (NSCSs) exhibit excellent mechanical properties due to the formation of a large volume fraction of ordered Ni<sub>3</sub>Al precipitates that are coherently embedded in the matrix of the Ni phase [1–4]. These ordered precipitates lead to order strengthening and anomalous temperature dependence of yield strength, thereby resulting in extraordinarily high strength and creep resistance at elevated temperatures [5].

As an intrinsic property of the materials with the  $L1_2$  structure [6, 7], the yield strength anomaly (YSA) is intimately connected to the stacking faults (SFs) in the (111) plane of Ni<sub>3</sub>Al, including the antiphase boundary (APB), the superlattice intrinsic stacking fault (SISF), and the complex stacking fault (CSF) [8]. For example, it was found that the thermally activated cross slip of screw dislocations from the {111} primary slip plane to the {001} cross slip plane is responsible for the YSA occurrence [9, 10], since the cross slip remains locked in Kear-Wilsdorf (KW) configurations [10]. The driving force to form the KW locks was found to be positively correlated with the APB energy ( $\gamma_{APB}$ ) [11] according to the Paidar-Pope-Vitek model [12]. Moreover, the KW locks tend to form when the CSF energy ( $\gamma_{CSF}$ ) is low [6, 13]. Furthermore, the dislocation ribbons of overall Burgers vector  $[\bar{1}12]$  shearing the Ni<sub>3</sub>Al precipitates can also affect the

YSA [14–17]. Specifically, at intermediate temperatures and high stresses, the  $[1\bar{1}0]$  dislocations first form in the matrix of the Ni phase and then decompose at the Ni/Ni<sub>3</sub>Al interface in the end of the first stage of creep or at the beginning of the second stage of creep [15]. The decomposition reaction can be described by  $1/2[011] + 1/2[\bar{1}01] \rightarrow 1/3[\bar{1}12] + 1/6[\bar{1}\bar{1}2]$  [15]. The leading partial dislocation  $1/3[\bar{1}12]$  enters the Ni<sub>3</sub>Al phase and creates a SISF, while the trailing partial dislocation  $1/6[\bar{1}\bar{1}2]$  remains at the Ni/Ni<sub>3</sub>Al interface [15]. The formation of the  $[\bar{1}12]$  dislocation ribbons was first observed by Leverant and Kear using transmission electron microscopy [18] and later confirmed by other studies [15, 16, 19, 20]. The SISF has a lower energy as compared to other SF configurations and was thought to be the dominant SF that drives the shearing of the Ni<sub>3</sub>Al phase under high stress and intermediate-temperature creep conditions [15, 21–24]. Besides, the formation of high-density SFs can promote the accumulation of partial dislocations, thereby enhancing both the ductility and fracture toughness but without compromising high strengths. Considering the significant effects of the SFs in improving the creep behavior of NSCSs, controllable tuning the SF energy by alloying would be highly desirable for the design of high-performance NSCSs.

Experimentally, it is tough to obtain an accurate value of the SF energy of NSCSs, because the separation distance between partial dislocations in electron microscope images is too small to identify [25, 26]. Based on the weak-beam method of electron microscopy, the derived SF energies of the Ni phase normally lie in the range of 120–130 mJ/m<sup>2</sup> [27, 28]. It is well known that to acquire high-performance NSCSs, more than

\* ptliu@imr.ac.cn

† xingqiu.chen@imr.ac.cn

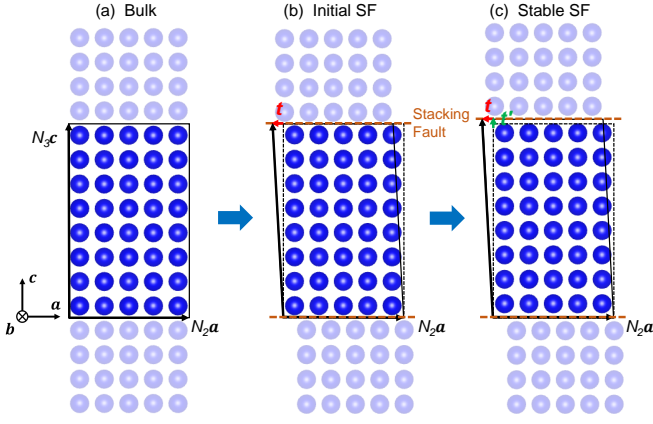


Figure 1. Sketch of stacking fault (brown dashed lines) modeled by the alias shear method. The lattice containing dark blue balls indicates the supercell used for calculating the GSFE. (a) Undistorted supercell viewed in the  $ac$  plane. (b) Initial supercell with an ideal stacking fault, which is created by  $N_3c \rightarrow N_3c + t$  with  $t$  being a displacement vector along the slip direction (here along  $a$ ). Note that the atomic positions remain fixed in their initial cartesian coordinates. (c) Supercell after structural relaxations along the  $c$  direction only. Here,  $t'$  denotes the change of the lattice vector along  $c$ .

ten alloying elements have been added to the NSCSs so far, such as Ti, V, Cr, Co, Zr, Nb, Mo, Ru, Hf, Ta, W and Re. For instance, it was experimentally found that Re and Co can reduce the SF energy of Ni [29]. Similar effects were obtained by other alloying elements such as Co, Cr, Mo, Ti and W [30, 31].

In contrast to experiments, theoretical calculations in particular the *ab initio* calculations based on the density functional theory (DFT) have demonstrated their increasing power in alloys design, providing important complementary perspectives in guiding the experimental studies [32–35]. As early as in the year of 1968, Vitek proposed the generalized stacking fault energy (GSFE) model to explain the effect of SF energy on shear deformation [36]. In this model, the local minimum and maximum of the GSFE along the pathway of slip system are regarded as stable stacking fault energy ( $\gamma_{sf}$ ) and unstable stacking fault energy ( $\gamma_{usf}$ ), respectively. In general, the low  $\gamma_{sf}$  can lead to a larger width of stacking faults [37], a higher strain-hardening coefficient [38], a higher twinnability [39, 40], a lower twinning stress [41] and a lower occurrence of cross-slip (or climb) [28, 42] as well as a lower steady-state creep rate [43–45]. The GSFE model combined with *ab initio* calculations has been widely adopted to study the effects of the alloying elements on the SF energies of Ni and Ni<sub>3</sub>Al [45–54]. For instance, Yu *et al.* [45] found that Mo, Re and W remarkably decrease the  $\gamma_{sf}$  of Ni due to the  $d$ - $d$  orbitals hybridizations between solute and Ni. Shang *et al.* [46, 47] obtained that almost all the alloying elements decrease the  $\gamma_{sf}$  of Ni, with the effect being more pronounced as the alloying element is far from Ni in the periodic table.

Although the effects of alloying elements on the SF energies of the Ni phase have been extensively studied [45–54],

they are normally done on a case-by-case basis and a systematic and thorough investigation of typical alloying elements in the periodic table is still lacking, in particular for the Ni<sub>3</sub>Al phase for which only a few alloying elements' effects on the SF energies have been reported [54]. The contribution of this work is to establish a general and exhaustive dictionary of the effects of various alloying elements on the GSFEs of different slip systems of both Ni and Ni<sub>3</sub>Al phases. This not only allows us to identify good strengthening alloying elements, but also enables to determine alternative alloying elements that exhibit similar strengthening effects. This is what the materials scientists desire and eventually would help to guide the design of the next-generation high-performance NSCSs.

This work is organized as follows. First, the computational model used to compute the GSFEs for various slip systems of the (111) plane of Ni and Ni<sub>3</sub>Al is introduced. Then, the GSFEs of the (111) plane of pure Ni and Ni<sub>3</sub>Al as well as their corresponding alloys are calculated. The focus is on elucidating the effects of the considered 29 alloying elements on the values of  $\gamma_{sf}$  and  $\gamma_{usf}$  of different slip systems. Finally, conclusions are drawn.

## II. METHODS AND COMPUTATIONAL DETAILS

All first-principles calculations were performed using the Vienna *ab initio* simulation package (VASP) [55, 56]. The generalized gradient approximation [57] parameterized by Perdew-Burke-Ernzerhof (PBE) was employed for the exchange-correlation functional. The plane wave cutoff energy was set to 420 eV and the Brillouin zone was sampled by a  $\Gamma$ -centered  $k$ -point grid with the smallest allowed spacing between  $k$  points of  $0.16 \text{ \AA}^{-1}$ . The convergence criteria for the total energy and ionic forces were set to  $10^{-6}$  eV and  $0.01 \text{ eV/\AA}$ , respectively. The first-order Methfessel-Paxton method [58] with a smearing width of  $0.18 \text{ eV}$  was used for structure relaxations, whereas the Blöchl-corrected tetrahedron method [59] was used to obtain more accurate total energies. For all the calculations, spin polarization was considered.

To calculate the GSFEs, two approaches for modeling the SFs have been proposed. The first one is the slab shear method [48, 60, 61] and the other one is the alias shear method [46, 47, 62, 63]. For the slab shear method, the SF is modeled by equally splitting a supercell into two slabs, where the atoms in the bottom slab are fixed, while the atoms in the upper slab undergo a certain displacement along the slip direction. By contrast, in the alias shear method the SF is complemented by an alias shear deformation of a periodic supercell lattice, whereas the atomic positions are still represented by the initial cartesian coordinates. As compared to the slab shear method, the required supercell for modeling the SF is reduced by a factor of two in the alias shear method, significantly decreasing the computational cost. For this reason, the alias shear method was employed to calculate the GSFEs throughout the work.

Figure 1 sketches the SF model using the alias shear method. First, a supercell with lattice vectors of  $N_1a$ ,  $N_2b$

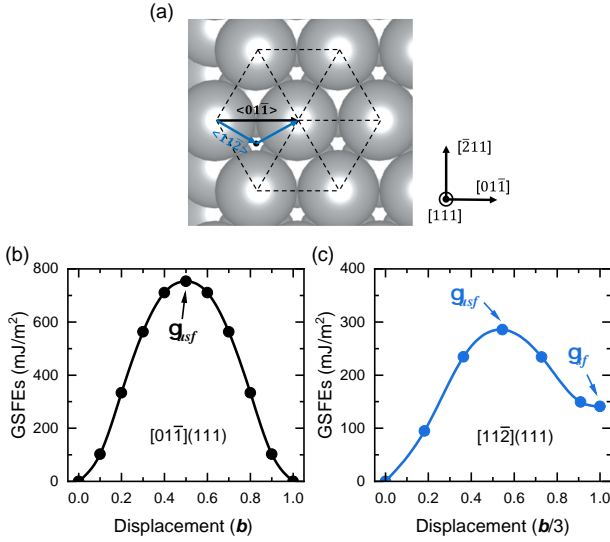


Figure 2. (a) Sketch of two slip systems of pure Ni, i.e.,  $[01\bar{1}](111)$  and  $1/3[11\bar{2}](111)$ . The corresponding GSFs are shown in (b) and (c).

and  $N_3c$  was built [Fig. 1(a)]. Then, a small vector  $t$  along the slip direction (here  $a$ ) was introduced on the lattice vector  $N_3c$ , which constructs a slip plane in the  $ab$  plane [see Fig. 1(b)]. Finally, the supercell (including both lattice vectors and atomic positions) was allowed to relax only along the  $c$  direction, giving rise to a net vector of  $t'$  perpendicular to the slip plane. Here, we employed a 96-atom orthorhombic supercell with the lattice vectors of  $[11\bar{2}]a_0$ ,  $2[\bar{1}10]a_0$ , and  $2[111]a_0$  with  $a_0$  being the lattice constant of conventional fcc unit cell. The length of the lattice vector along the  $[111]$  direction ensures to eliminate interactions between periodic stacking faults planes. The GSF was calculated by

$$\gamma_{GSF} = (E_{GSF} - E_0)/A, \quad (1)$$

where  $E_{GSF}$  and  $E_0$  represent the total energies of the supercell with or without the SF, respectively, and  $A$  is the area of the slip plane within the supercell. In order to calculate the  $\gamma_{GSF}$  with an alloying element, for  $Ni_{95}X$  we substituted one of Ni atoms in the GSF plane with an alloying element. Meanwhile, we also replaced a Ni atom in the GSF-free supercell. Since the solute is placed in the stacking fault plane, this translates to a planar solute concentration of 6.25 at.%. Similar procedure was performed for  $Ni_{72}Al_{23}X$ , but here only the substitution of Al atom in the GSF plane was considered due to its overall small normalized transfer energy as compared to that when substituting Ni atom [64–66].

### III. RESULTS AND DISCUSSION

#### A. The GSFs of pure Ni and $Ni_3Al$

Let us start from the pure Ni system. For the pure Ni, there are two typical slip systems, i.e.,  $[01\bar{1}](111)$  and  $[11\bar{2}](111)$

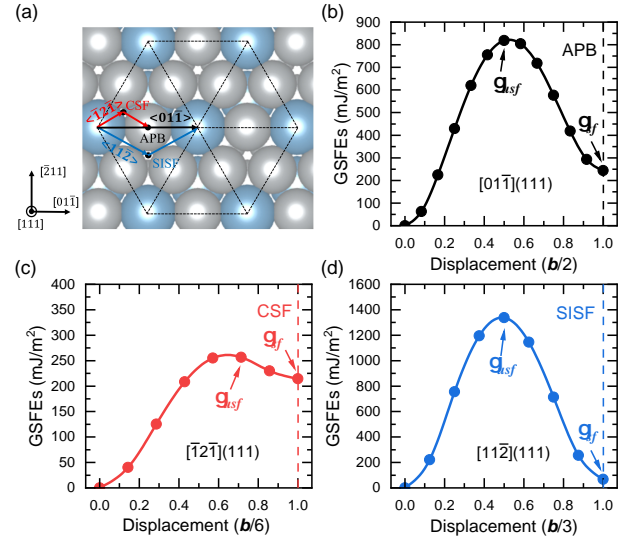


Figure 3. (a) Sketch of three slip systems of pure  $Ni_3Al$ , i.e.,  $[01\bar{1}](111)$ ,  $[12\bar{1}](111)$  and  $[11\bar{2}](111)$ . The corresponding GSFs are shown in (b), (c) and (d).

[see Fig. 2(a)]. The corresponding calculated GSFs are given in Table I and further plotted in Figs. 2(b) and (c). The  $\gamma_{usf}$  along the  $[01\bar{1}]$  direction is computed to be  $755 \text{ mJ/m}^2$ , which appears at  $b/2$  burgers vector, whereas the calculated  $\gamma_{usf}$  along the  $[11\bar{2}]$  direction appearing at  $b/6$  burgers vector is much smaller ( $285 \text{ mJ/m}^2$ ). This indicates that launching the  $[11\bar{2}](111)$  slip system would be easier as compared to the  $[01\bar{1}](111)$  slip system. This is consistent with the Rice criterion  $D = 0.3\gamma_{surf}/\gamma_{usf}$  [ $\gamma_{surf}$  is the surface energy,  $1906 \text{ mJ/m}^2$  for  $Ni(111)$ ] showing that the larger the  $D$  value is (equivalently smaller  $\gamma_{usf}$ ), the more ductile is the slip system [67]. Our calculated  $\gamma_{sf}$  and  $\gamma_{usf}$  are overall in line with the literature theoretical and experimental data (see Table I).

Next, we move to the pure  $Ni_3Al$  system. For the pure  $Ni_3Al$ , three inequivalent slip systems exist on the (111) plane, i.e.,  $[01\bar{1}](111)$ ,  $[12\bar{1}](111)$  and  $[11\bar{2}](111)$  [see Fig. 3(a)], due to the symmetry lowering as compared to Ni. Slipping the system along these directions by  $b/2$ ,  $b/6$  and  $b/3$  burgers vectors results in the formation of the APB, CSF and SISF, respectively. The corresponding calculated GSFs are given in Table I and further shown in Figs. 3(b)-(d). It can be seen that the  $\gamma_{usf}$  for forming CSF ( $257 \text{ mJ/m}^2$ ) is much lower than  $\gamma_{usf}$  for forming APB ( $819 \text{ mJ/m}^2$ ). These results support the decomposition reaction of a  $1/2\langle 1\bar{1}0 \rangle$  dislocation into two Shockley partials on the (111) plane of  $Ni_3Al$ , which can be described by  $1/2\langle 01\bar{1} \rangle \rightarrow 1/6\langle 12\bar{1} \rangle + 1/6\langle 11\bar{2} \rangle$  [8] [see red arrows in Fig. 3(a)]. Thus, the  $[12\bar{1}]$  direction exhibits the best ductility. Moreover, the SISF exhibits the smallest  $\gamma_{sf}$  of  $68 \text{ mJ/m}^2$ , much smaller than those of APB ( $244 \text{ mJ/m}^2$ ) and CSF ( $214 \text{ mJ/m}^2$ ). However, its formation needs to overcome the largest energy barrier ( $\gamma_{usf}=1339 \text{ mJ/m}^2$ ), where the  $\gamma_{usf}$  decreases in a sequence of  $[11\bar{2}](111) > [01\bar{1}](111) > [12\bar{1}](111)$ . This suggests that once SISF is produced, it is fairly kinetically stable and its slipping becomes much more

Table I. Calculated stable stacking fault energies ( $\gamma_{sf}$ ) and unstable stacking fault energies ( $\gamma_{usf}$ ) of different slip systems in Ni and Ni<sub>3</sub>Al, which are compared to other literature data.

Slip system	$\gamma_{sf}$ (mJ/m <sup>2</sup> )	$\gamma_{usf}$ (mJ/m <sup>2</sup> )	Notes and references
Ni: [01 $\bar{1}$ ](111)		755	Calc., this work, alias shear
		783	Calc., DFT, alias shear [52]
Ni: [11 $\bar{2}$ ](111)	141	285	Calc., this work, alias shear
	160	283	Calc., DFT, alias shear [52]
	149	273	Calc., DFT, slab shear [53]
	129	278	Calc., DFT, slab shear [51]
	120 ~ 130		Expt., weak-beam TEM images [27]
Ni <sub>3</sub> Al: [01 $\bar{1}$ ](111) (APB)	244	819	Calc., this work, alias shear
	259	830	Calc., DFT, alias shear [52]
	198	791	Calc., DFT, slab shear [53]
	180	778	Calc., DFT, slab shear [49]
	210		Calc., Peierls-Nabarro model [24]
	175±15		Expt., weak-beam TEM images [6]
Ni <sub>3</sub> Al: [ $\bar{1}$ 2 $\bar{1}$ ](111) (CSF)	214	257	Calc., this work, alias shear
	249		Calc., DFT, alias shear [52]
	208	227	Calc., DFT, slab shear [53]
	205	254	Calc., DFT, slab shear [49]
	225		Calc., Peierls-Nabarro model [24]
	235±45		Expt., weak-beam TEM images [6]
Ni <sub>3</sub> Al: [11 $\bar{2}$ ](111) (SISF)	68	1339	Calc., this work, alias shear
	47	1421	Calc., DFT, alias shear [52]
	21	1332	Calc., DFT, slab shear [53]
	75	1368	Calc., DFT, slab shear [49]
	80		Calc., Peierls-Nabarro model [24]
	6±0.5		Expt., weak-beam TEM images [6]
	35		Expt., weak-beam TEM images [19]

difficult. This might be connected with the anomalous temperature dependence behaviour of the YSA [15, 21–24]. Our predictions are in reasonable agreement with other DFT calculations and experimental estimations (see Table I). The noticeable exception is that the experimentally estimated  $\gamma_{sf}$  of SISF from Karnthaler *et al.* [6] using weak-beam TEM images is somewhat too small ( $6 \pm 0.5$  mJ/m<sup>2</sup>). However, the more recent experimental estimation by Knowles and Chen [19] using the same technique obtained a much larger value (35 mJ/m<sup>2</sup>) that is in better agreement with the DFT calculated results.

### B. Effects of alloying elements on the $\gamma_{usf}$ and $\gamma_{sf}$ of Ni

To explore the effects of the alloying elements on the  $\gamma_{usf}$  and  $\gamma_{sf}$  of different slip systems in Ni, twenty-nine alloying elements including most of transition-metal elements and Ce were considered. Figure 4 shows the calculated  $\gamma_{usf}$  and  $\gamma_{sf}$  with the addition of an alloying element on the SF plane. The detailed values are summarized in Table II. First, it is interesting to see that the calculated  $\gamma_{usf}$  for the [01 $\bar{1}$ ](111) and [11 $\bar{2}$ ](111) slip systems exhibit similar trends as the atomic number of alloying elements increases along

the period [Figs. 4(a) and (c)]. Specifically, as the element moves from the left to the right along the period, the  $\gamma_{usf}$  first increases, then reaches the maximum around group VIII elements, and eventually decrease as the atomic number increases further. Second, as compared to Ni, most of alloying elements tend to reduce  $\gamma_{usf}$  except for Cr, Mn, Fe, Co, Re and Os [see Figs. 4(a) and (c)]. Moreover, the alloying elements in the 5th and 6th periods are found to exhibit more pronounced effects in decreasing  $\gamma_{usf}$  than those in the 4th period. In particular, Ce shows the strongest reduction of  $\gamma_{usf}$ . This indicates that the addition of alloying elements in Ni render the deformation of [01 $\bar{1}$ ](111) and [11 $\bar{2}$ ](111) slip systems more easily.

Moving to the  $\gamma_{sf}$  for the [11 $\bar{2}$ ](111) slip system, one can observe from Fig. 4(e) that all alloying elements decrease the  $\gamma_{sf}$ , with the effect being more pronounced as the alloying elements are far from Ni in the periodic table. Similar to the effects of alloying elements on  $\gamma_{usf}$ , the alloying elements in 5th and 6th periods also decrease  $\gamma_{sf}$  more remarkably than the 4th period elements. Although the elements in groups VIB-VIIB and the first two columns of group VIII almost have a negligible effect (just  $\pm 2\%$  reduction) on the  $\gamma_{usf}$  along the [01 $\bar{1}$ ] and [11 $\bar{2}$ ] directions, they have a considerable effect



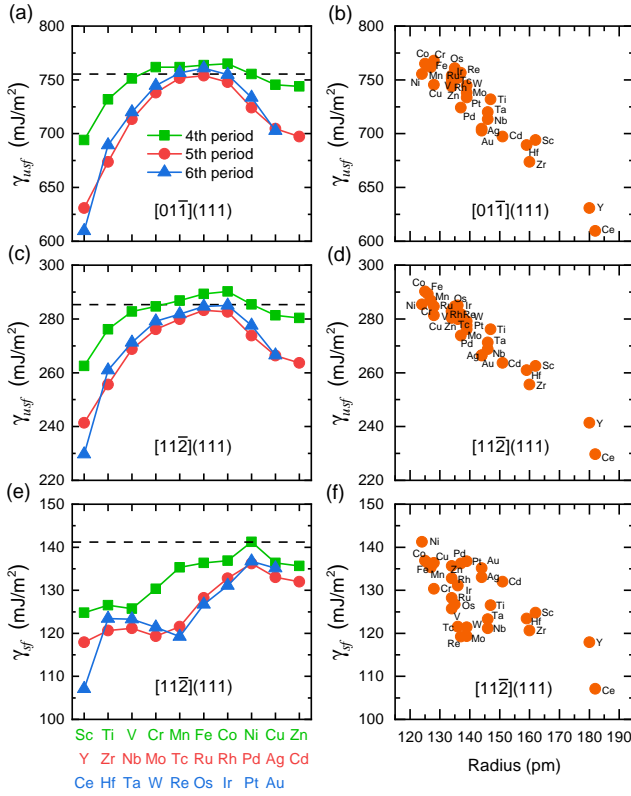


Figure 4. The effects of considered alloying elements on the GSFs of Ni for the slip systems of (a)  $\gamma_{usf}$  of  $[01\bar{1}](111)$  (c)  $\gamma_{usf}$  of  $[11\bar{2}](111)$  and (e)  $\gamma_{sf}$  of  $[11\bar{2}](111)$ . (b), (d) and (f) show the corresponding GSFs as a function of the radii of alloying elements. The dashed line represents the  $\gamma_{usf}$  and  $\gamma_{sf}$  of pure Ni.

(about  $\pm 15\%$  reduction) on the  $\gamma_{sf}$  of  $[11\bar{2}](111)$  slip system. It is interesting to observe that as compared to the elements in the same period, Mo and Re exhibit unusual reduction of  $\gamma_{sf}$  due to their  $d-d$  orbitals hybridizations with Ni [45]. These results are consistent with the findings of Shang *et al.* [46]. Since a small value of SF results in a low steady-state creep rate [43–45], one can thus expect that the addition of Ce, Y, Re and Mo in Ni can improve creep resistance and exhibit good solid solution strengthening effect.

Figures 4(b), (d) and (f) show the calculated  $\gamma_{usf}$  and  $\gamma_{sf}$  of different slip systems as a function of the atomic radii of alloying elements. It is evident that the  $\gamma_{usf}$  follows a linear behavior with respect to atomic radii and the alloying elements with larger atomic radii in general exhibit more pronounced reduction effect on  $\gamma_{usf}$ . Among the considered elements, the effects of Y and Ce are strongest, due to their large atomic radii difference with respect to that of Ni. However, for  $\gamma_{sf}$  the degree of linear correlation with atomic radii is relatively decreased. These results suggest that the strain effects induced by alloying elements play a dominant role in reducing the  $\gamma_{usf}$  and  $\gamma_{sf}$  of Ni, which are responsible for the trends manifested in Figs. 4(a), (c) and (e).

One note is in place here before closing this section. We recall that with our employed supercell model the planar solute

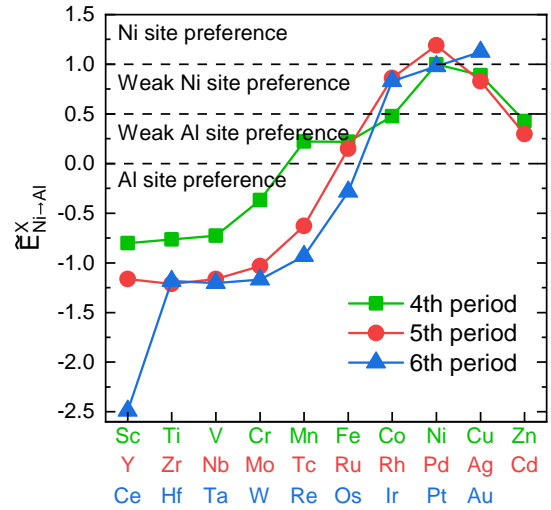


Figure 5. Calculated normalized transfer energies of 29 alloying elements.

concentration is 6.25 at.%. Therefore, strictly speaking, our results and discussions apply to the situation of dilute solute concentration. Exploring the effects of solute concentration on the GSFs is, however, computationally too demanding for all considered 29 alloying elements due to the rapid increase of configuration space, and is beyond the scope of the present work. We shall also stress that in our work we focus only on the general trends of the effects of different alloying elements on the GSFs of Ni and  $Ni_3Al$ . Despite of this, it would still be interesting to see to what extent the trends obtained from our calculations in dilute solute concentration apply to higher solute concentrations. To this end, we compared our results in Fig. A1 of the Appendix to the available literature data for Al, Ti, Cr and Co that were obtained using a relatively small supercell model [45, 46, 68]. Since the variations of stacking fault energies were found to almost follow a linear behavior with the solute concentration, the overall trends across different alloying elements remain unchanged with the modification of solute concentrations, i.e., in a sequence of  $Ti > Cr > Al > Co$  for reducing the stacking fault energy (see Fig. A1). In this regard, we can say that the results obtained from our work still have a certain extrapolation capability to the not high solute concentration regime. However, whether this still holds for other alloying elements remains to be carefully examined.

### C. Effects of alloying elements on the $\gamma_{usf}$ and $\gamma_{sf}$ of $Ni_3Al$

When an alloying element is added to ordered  $Ni_3Al$  phase, it can either substitute the Ni site or the Al site. Hence, one needs to first determine the site preference of alloying elements before discussing their effects on the  $\gamma_{usf}$  and  $\gamma_{sf}$ . To this end, we employed the Wagner-Schottky model [65, 69]. In this model, the site preference can be determined by the

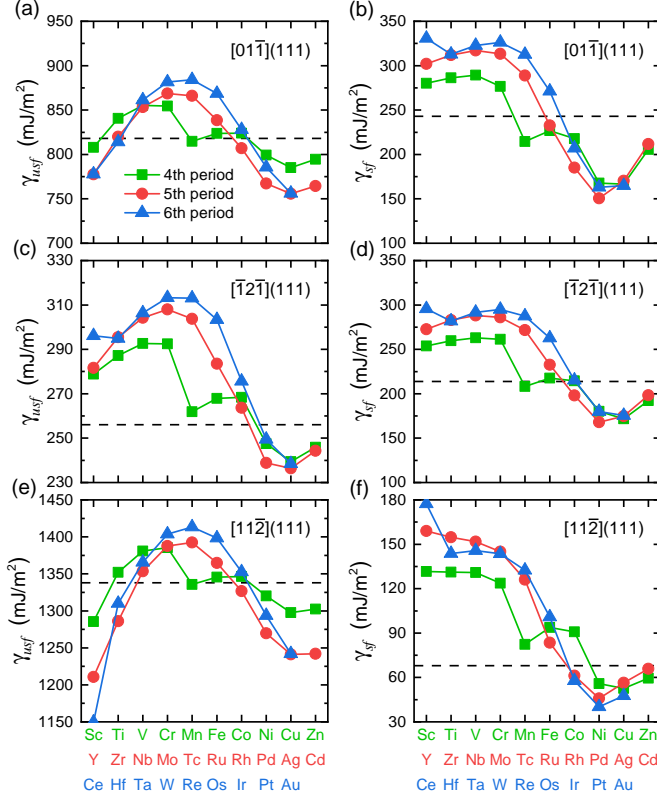


Figure 6. The effects of considered alloying elements on the  $\gamma_{usf}$  (left panels) and  $\gamma_{sf}$  (right panels) of  $\text{Ni}_3\text{Al}$  for the slip systems of  $[01\bar{1}](111)$  [(a) and (b)],  $[\bar{1}2\bar{1}](111)$  [(c) and (d)], and  $[11\bar{2}](111)$  [(e) and (f)]. The dashed line represents the  $\gamma_{usf}$  and  $\gamma_{sf}$  of pure  $\text{Ni}_3\text{Al}$ .

normalized transfer energy

$$\tilde{E}_{\text{Ni} \rightarrow \text{Al}}^X = E_{\text{Ni} \rightarrow \text{Al}}^X / E_{\text{anti}}, \quad (2)$$

where  $E_{\text{anti}}$  is the sum of the formation energy of an Al antisite defect and that of a Ni antisite defect.  $E_{\text{Ni} \rightarrow \text{Al}}^X$  is the transfer energy that an alloying element ( $X$ ) transfers from a Ni site to an Al site, and at the same time, the Al atom goes to the Ni site where the  $X$  atom initially occupied. The transfer energy is defined as

$$E_{\text{Ni} \rightarrow \text{Al}}^X = E^X(\text{Al}) + E^{\text{Al}}(\text{Ni}) - E^X(\text{Ni}) - E_{\text{Ni}_3\text{Al}}, \quad (3)$$

where  $E^X(\text{Al})$  and  $E^X(\text{Ni})$  are the total energies of  $\text{Ni}_3\text{Al}$  with a  $X$  atom at Al and Ni sites, respectively,  $E^{\text{Al}}(\text{Ni})$  is the total energy of  $\text{Ni}_3\text{Al}$  with an Al antisite, and  $E_{\text{Ni}_3\text{Al}}$  is the total energy of pure  $\text{Ni}_3\text{Al}$ . According to the Wagner-Schottky model, one can obtain that, if  $\tilde{E}_{\text{Ni} \rightarrow \text{Al}}^X < 0$ , the solute  $X$  has a strong tendency to occupy the Al site, if  $\tilde{E}_{\text{Ni} \rightarrow \text{Al}}^X > 1.0$ , the solute has a strong tendency to occupy the Ni site, if  $0 < \tilde{E}_{\text{Ni} \rightarrow \text{Al}}^X < 0.5$ , the solute has a weak Al site preference, and if  $0.5 < \tilde{E}_{\text{Ni} \rightarrow \text{Al}}^X < 1.0$ , the solute has a weak Ni site preference.

Figure 5 shows the calculated normalized transfer energies of 29 alloying elements. It is evident that Sc, Ti, V, Cr, Y,

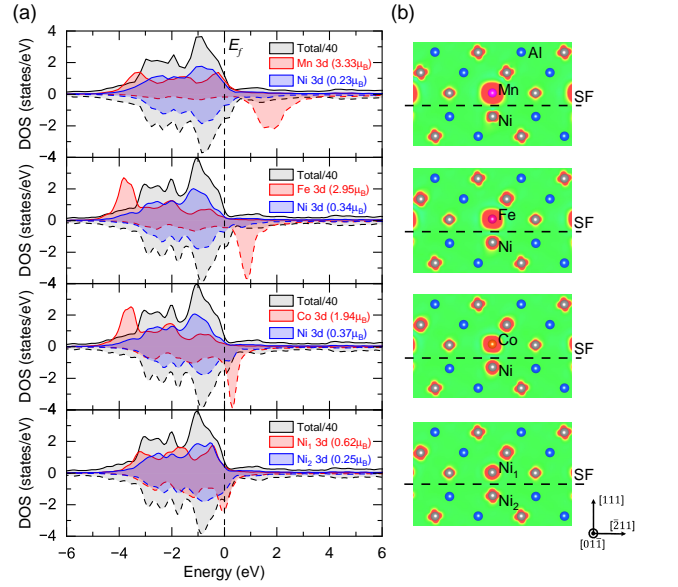


Figure 7. (a) Spin-polarized local density of states (LDOSs) of alloying elements (Mn, Fe, Co and Ni) and their first-nearest neighboring Ni atom for the configuration used to calculate  $\gamma_{usf}$  of  $[11\bar{2}](111)$  slip in  $\text{Ni}_3\text{Al}$ . The atomic positions are indicated in (b). The Fermi energy has been aligned to zero. For a better presentation, the total DOSs have been divided by a factor of 40. The values in parentheses represent the calculated magnetic moments. (b) The corresponding spin density isosurface (with an iso-value of  $0.01 \text{ e}/\text{\AA}^3$ ) for the  $(01\bar{1})$  plane including the alloying elements.

Zr, Nb, Mo, Tc, Ce, Hf, Ta, W, Re, and Os show a strong Al site preference, while Pd, Pt, and Au exhibit a strong Ni site preference. Mn, Fe, Co, Zn, Ru, and Cd display a weak Al site preference, whereas Cu, Rh, Ag, and Ir show a weak Ni site preference. Our results are consistent with previous studies based on the Wagner-Schottky model [64–66, 70, 71] and also agree well with the findings of Chen *et al.* [13] using a grand canonical dilute-solution model thermodynamic formalism. In addition, the fact that Ti, Cr, Nb, Ta, W, and Re favor to occupy the Al site in  $\text{Ni}_3\text{Al}$  agrees well with previous first-principles calculations based Monte-Carlo simulations [72, 73] as well as the widely accepted experimental recognition [1, 74]. We note that the elements with  $0 < \tilde{E}_{\text{Ni} \rightarrow \text{Al}}^X < 1$  exhibit a strong composition-dependent site preference. For instance, they prefer to occupy the Ni site in Al-rich  $\text{Ni}_3\text{Al}$ , but favor to occupy the Al site in Ni-rich  $\text{Ni}_3\text{Al}$ , while in stoichiometric  $\text{Ni}_3\text{Al}$  they show no site preference such that they randomly occupy the Al and Ni sites [13, 50].

Considering that most of alloying elements tend to occupy the Al site in  $\text{Ni}_3\text{Al}$ , in the following we focus on the effects of the alloying element occupying the Al site on the  $\gamma_{usf}$  and  $\gamma_{sf}$  for three inequivalent slip systems. The results are presented in Fig. 6 and summarized in Table II. It is interesting to find that the effects of alloying elements on  $\gamma_{usf}$  or  $\gamma_{sf}$  follow a similar trend for three slip systems. Taking  $\gamma_{usf}$  for example, when the element moves from left to right in the same period, the  $\gamma_{usf}$  in general first increases, then reaches the maximum,

and finally goes down. For the elements in groups VB-VIIB and the first column of group VIII, they have a striking impact on  $\gamma_{usf}$  (except for Mn and Fe) [see Figs. 6(a), (c) and (e)]. Especially, the elements W and Re in the 6th period and Mo in the 5th period significantly increase the values of  $\gamma_{usf}$ . Since large  $\gamma_{usf}$  values make dislocation emits and plastic deformation more difficult [45], one can expect that the addition of these elements to Ni<sub>3</sub>Al can hinder the slip deformation. On the other hand, the elements in groups IB-IIIB and the last column of group VIII have a negative effect on  $\gamma_{usf}$ , in particular the elements Cu, Ag, and Au in group IB, indicating that these elements can improve the slip deformation of Ni<sub>3</sub>Al.

For  $\gamma_{sf}$ , the elements in groups IIIB-VIIB (except for Mn) increase  $\gamma_{sf}$ , especially the elements Ce, W and Re. This means that these elements reduce the stability of the APB configuration in the  $[01\bar{1}](111)$  slip system, the CSF configuration in the  $[\bar{1}2\bar{1}](111)$  slip system, and the SISF configuration in the  $[11\bar{2}](111)$  slip system. Our results are consistent with the findings of Yu *et al.* [45, 53]. Since small values of SF lower the steady-state creep rate [43–45], the elements in groups IIIB-VIIB would thus reduce the creep strength of Ni<sub>3</sub>Al.

By examining calculated  $\gamma_{usf}$  and  $\gamma_{sf}$  of Ni<sub>3</sub>Al versus atom radii (not shown), we found that they do not simply follow a linear behavior as the case in Ni. Thus, besides the strain effects, electronic structures changed by the alloying elements also take effects in determining the values of  $\gamma_{usf}$  and  $\gamma_{sf}$  for Ni<sub>3</sub>Al. Furthermore, one notices that among the considered elements, Mn, Fe and Co exhibit abnormal behaviors (see Fig. 6). Our electronic structure analysis demonstrates that these abnormal behaviors originate from their strong spin polarizations. Just taking  $\gamma_{usf}$  of  $[11\bar{2}](111)$  slip in Ni<sub>3</sub>Al as an example, we plot in Fig. 7 the LDOSs of alloying elements (Mn, Fe, Co and Ni) and their first-nearest neighboring Ni atom as well as corresponding spin density isosurfaces. It is evident that the spin polarization decreases in the order of Mn, Fe, Co and Ni, yielding local magnetic moments of 3.33  $\mu_B$ , 2.95  $\mu_B$ , 1.94  $\mu_B$  and 0.62  $\mu_B$ , respectively. By contrast, the other alloying elements do not exhibit magnetic couplings with the neighboring Ni atoms.

#### D. Effects of alloying elements on normal slip barriers

The slip deformation is a reaction process with an energy barrier ( $\gamma_{usf}$ ) to overcome to form stable SFs, whose stability is described by  $\gamma_{sf}$ . In order to better describe the effects of alloying elements on the SFs, here, we defined the process from a perfect supercell slip to the formation of a stable SF configuration as the leading slip process (LSP) and its inverse process was defined as the tailing slip process (TSP) [see Fig. 8(a)]. We notice that simply comparing  $\gamma_{sf}$  and  $\gamma_{usf}$  is not sufficient to capture the overall effects of different alloying elements on GSFs in an accurate manner. To address this issue, we have proposed renormalized  $R_1 = \gamma_{usf}^X / \gamma_{usf}^0$  and  $R_2 = (\gamma_{usf}^X - \gamma_{sf}^X) / (\gamma_{usf}^0 - \gamma_{sf}^0)$  indices to effectively characterize the effects of alloying elements on the slip barriers of the LSP and TSP, respectively. Here,  $\gamma_{usf}^X$  and  $\gamma_{usf}^0$  represent

the unstable stacking fault energies with and without alloying element X, respectively, whereas  $\gamma_{sf}^X$  and  $\gamma_{sf}^0$  denote the stable stacking fault energies with and without alloying element X, respectively. According to this definition, one can obtain that the indices  $R_1$  ( $R_2$ ) greater than 1 mean that the alloying elements increase the barrier of the LSP (TSP), which makes deformation more difficult. On the contrary, when the indices are less than 1, the deformation becomes easier with the addition of alloying elements. In this way, the different alloying elements with similar effects can well be classified into the same  $R_1$ - $R_2$  quadrant.

The clarification results are compiled in Fig. 8 in terms of  $R_1$  and  $R_2$ . From the plot it is evident that among all considered alloying elements Re is an excellent strengthening element that significantly increases the barrier of the TSP of the  $[01\bar{1}](111)$  slip system for the Ni phase, and also enhances the barrier of the LSP of the  $[01\bar{1}](111)$ ,  $[\bar{1}2\bar{1}](111)$ ,  $[11\bar{2}](111)$  three slip systems for the Ni<sub>3</sub>Al phase. However, it shows a negligible or even slight negative impact on the LSP of  $[01\bar{1}](111)$  slip system in Ni and the TSP of  $[\bar{1}2\bar{1}](111)$  slip system in Ni<sub>3</sub>Al. We note that W and Mo exhibit similar effects as Re. The element of Os is almost distributed in the red area (see Fig. 8), which suggests that it shows strengthening effects on both LSP and TSP for Ni and Ni<sub>3</sub>Al. Our findings are consistent with the design strategy recently proposed by Bensheng *et al.* [75] who suggested to replace Re by Os in order to improve creep resistance and phase stability of nickel-based single crystal superalloys. It turns out that the newly designed Os-containing superalloy indeed shows a lower creep rate than commercial Re-containing CMSX-4 alloy at 980 °C/200 MPa/100 hours [75]. In addition, we found that Ru and Ir exhibit similar effects as Os. This might explain why the Ru element has been included in the fourth-generation (EPM-102 [76] and TMS-138 [77]) and fifth-generation NSCSs (TMS-173 [78]), and the Ir element has been included in the sixth-generation NSCSs (TMS-238 [79, 80]). By contrast, the rare-earth elements Y and Ce dramatically decrease  $R_1$  and  $R_2$ , indicating that they are not good alloying elements for improving the slip barrier of Ni or Ni<sub>3</sub>Al. Despite of this, a certain amount of Y or Ce has been added to superalloys because of their strong deoxidizing and desulfurizing abilities [81].

#### IV. CONCLUSIONS

In summary, we have systematically studied the effects of 29 alloying elements on the GSFs of different slip systems in Ni and Ni<sub>3</sub>Al through a comprehensive first-principles calculations based on the alias shear method. The conclusions drawn from this study are as follows:

(i) For Ni, except for magnetic elements Mn, Fe and Co, most of alloying elements decrease  $\gamma_{usf}$  of  $[01\bar{1}](111)$  and  $[11\bar{2}](111)$  slip systems and also decrease  $\gamma_{sf}$  of the  $[11\bar{2}](111)$  slip system. The reduction effects show a strong correlation with the inverse of atom radii.

(ii) For Ni<sub>3</sub>Al, most of alloying elements in groups IIIB-VIIB show a strong Al site preference. Except for Mn and

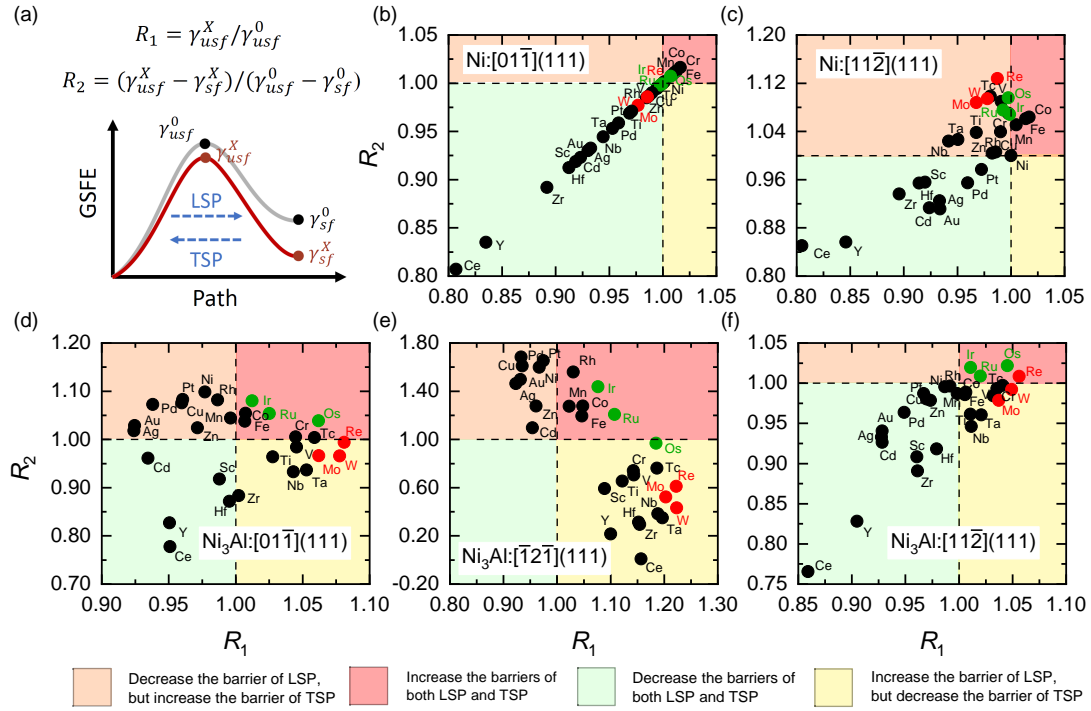


Figure 8. (a) Sketch of the GSFE curve along a slip path with the LSP and TSP being indicated. (b)-(f) A summary of the effects of alloying elements on the barriers of LSP and TSP for different slip systems in Ni and Ni<sub>3</sub>Al. (b) Ni: [011̄](111), (c) Ni: [112̄](111), (d) Ni<sub>3</sub>Al: [011̄](111), (e) Ni<sub>3</sub>Al: [121̄](111), (f) Ni<sub>3</sub>Al: [112̄](111).

Fe, the elements in groups VB-VIIB and the first column of group VIII increase the value of  $\gamma_{usf}$  of different slip systems of the Ni<sub>3</sub>Al phase, which makes the slip deformation and dislocation emits difficult. However, the elements in groups IIIB-VIIB also increase the value of  $\gamma_{sf}$ , and thus reduce the stability of APB, CSF and SISF configuration of the Ni<sub>3</sub>Al phase.

(iii) The alloying elements have been suitably clarified into four quadrants in terms of the two proposed indices  $R_1$  and  $R_2$  (see Fig. 8). We obtained that Re is an excellent strengthening alloying element that significantly increases the slip barrier of the trailing slip process for the Ni phase, and also enhances the slip barrier of the leading slip process of three slip systems for

the Ni<sub>3</sub>Al phase. W and Mo exhibit similar effects as Re.

(iv) We predicted that Os, Ru, and Ir are also good strengthening alloying elements, which show the strengthening effects on both the leading and trailing slip processes for Ni and Ni<sub>3</sub>Al.

We anticipate that our established dictionary of the effects of various alloying elements on the GSFEs of both Ni and Ni<sub>3</sub>Al phases and new findings would be appreciated by the broad community for guiding the design of the next-generation high-performance Ni-based single crystal superalloys.

Table II: A summary of calculated stable stacking fault energies ( $\gamma_{sf}$ ) and unstable stacking fault energies ( $\gamma_{usf}$ ) of different slip systems in Ni and Ni<sub>3</sub>Al with the addition of alloying elements. The available literature data are also given.

Elements	Ni: [01 $\bar{1}$ ](111)	Ni: [11 $\bar{2}$ ](111)	Ni <sub>3</sub> Al: [01 $\bar{1}$ ](111)	Ni <sub>3</sub> Al: [ $\bar{1}$ 2 $\bar{1}$ ](111)	Ni <sub>3</sub> Al: [11 $\bar{2}$ ](111)				
	$\gamma_{usf}$	$\gamma_{usf}$	$\gamma_{sf}$	$\gamma_{usf}$	$\gamma_{sf}(\gamma_{APB})$	$\gamma_{usf}$	$\gamma_{sf}(\gamma_{CSF})$	$\gamma_{usf}$	$\gamma_{sf}(\gamma_{SISF})$
Sc	694	263	125	808	280	279	254	1285	132
			108 [46]						
Ti	732	276	127	841	286	287	260	1352	131
			113 [46]	839[49]		308[49]		1438[49]	
V	751	283	126	855	289	293	263	1381	131
			113[46]						
Cr	768	285	130	855	277	292	261	1385	124
		248[51]	119 [46], 110[51], 107[45]						



(Continued)

Elements	Ni: $[01\bar{1}](111)$	Ni: $[11\bar{2}](111)$		Ni <sub>3</sub> Al: $[01\bar{1}](111)$		Ni <sub>3</sub> Al: $[\bar{1}2\bar{1}](111)$		Ni <sub>3</sub> Al: $[11\bar{2}](111)$	
	$\gamma_{usf}$	$\gamma_{usf}$	$\gamma_{sf}$	$\gamma_{usf}$	$\gamma_{sf}(\gamma_{APB})$	$\gamma_{usf}$	$\gamma_{sf}(\gamma_{CSF})$	$\gamma_{usf}$	$\gamma_{sf}(\gamma_{SISF})$
Mn	762	287	135	815	215	262	208	1336	82
		274[48]	124 [46], 86[48]						
Fe	764	289	136	824	227	268	218	1345	94
		280[48]	125 [46], 86[48]						
Co	765	290	137	824	218	268	215	1347	91
		234[51]	127 [46], 110[51], 124[45]						
Ni	755	285	141	799	168	247	180	1320	56
			132 [46]						
Cu	745	281	136	785	167	239	172	1298	53
		256[48]	126 [46], 86[48]						
Zn	744	280	136	795	206	246	192	1302	59
			125 [46]						
Y	631	241	118	778	302	282	273	1211	159
	589[52]	220[52]	96 [46], 130[52]	731[52]	302[52]			1083[52]	81[52]
Zr	674	256	121	820	312	295	283	1286	155
	656[52]	244[52]	101 [46], 135[52]	858[52]	365[52]			1350[52]	316[52]
Nb	713	269	121	853	317	304	288	1353	152
		223[48]	104[46], 59[48]						
Mo	738	276	119	869	313	308	286	1388	145
		280[53]	103[46], 55[53], 100[45]	1034[53]	531[53]			1553[53]	238[53]
Tc	752	280	122	866	289	304	272	1393	126
			105[46]						
Ru	754	283	128	839	233	284	233	1365	83
		308[53]	116[46], 95[53], 108[45]	905[53], 837[49]	185[53]	339[53], 294[49]	242[53]	1456[53], 1350[49]	29[53]
Rh	748	283	133	807	185	264	198	1327	61
			122[46]						
Pd	724	274	136	767	151	239	168	1270	46
			127[46]						
Ag	705	266	133	756	170	236	175	1241	56
Cd	697	264	132	764	212	244	198	1242	66
Ce	610	230	107	778	331	296	296	1149	177
Hf	689	261	123	814	313	295	282	1310	144
	689[52]	253[52]	106[46], 140[52]	914[52]	373[52]			1404[52]	300[52]
Ta	720	271	123	861	323	306	292	1366	146
		276[53]	108[46], 86[53]	1013[53], 908[49]	585[53]	588[53], 337[49]	394[53]	1479[53], 1470[49]	347[53]
W	745	279	121	881	326	313	295	1404	144

(Continued)

Elements	Ni: [01 $\bar{1}$ ](111) $\gamma_{usf}$	Ni: [11 $\bar{2}$ ](111) $\gamma_{usf}$	Ni: [11 $\bar{2}$ ](111) $\gamma_{sf}$	Ni <sub>3</sub> Al: [01 $\bar{1}$ ](111) $\gamma_{usf}$	Ni <sub>3</sub> Al: [01 $\bar{1}$ ](111) $\gamma_{sf}(\gamma_{APB})$	Ni <sub>3</sub> Al: [1 $\bar{1}$ 2](111) $\gamma_{usf}$	Ni <sub>3</sub> Al: [1 $\bar{1}$ 2](111) $\gamma_{sf}(\gamma_{CSF})$	Ni <sub>3</sub> Al: [11 $\bar{2}$ ](111) $\gamma_{usf}$	Ni <sub>3</sub> Al: [11 $\bar{2}$ ](111) $\gamma_{sf}(\gamma_{SISF})$
		257[48], 289[53]	105[46], 38[48], 59[53], 103[45]	1094[53], 939[49]	599[53]	611[53], 350[49]	425[53]	1636[53], 1531[49]	281[53]
Re	757	282 301[53]	119 103[46], 48[53], 100[45]	884 1079[53], 941[49]	313 494[53]	313 524[53], 366[49]	287 432[53]	1413 1628[53], 1533[49]	132 142[53]
Os	761	285	127 113[46]	869	271	303	263	1398	101
Ir	755	285	131 120[46]	828	207	276	215	1353	58
Pt	734	278	137 128[46]	786	163	249	180	1294	40
Au	703	266	135	756	165	238	176	1242	48

## ACKNOWLEDGMENTS

This work was supported by the National Key R&D Program of China (No. 2021YFB3501503), the National Science Fund for Distinguished Young Scholars (No. 51725103), and the funding of National Science and Technology Major Project (J2019-VI-0004-0118, J2019-VI-0019-0134). All calculations were performed on the high performance computational cluster at the Shenyang National University Science and Technology Park.

## Appendix

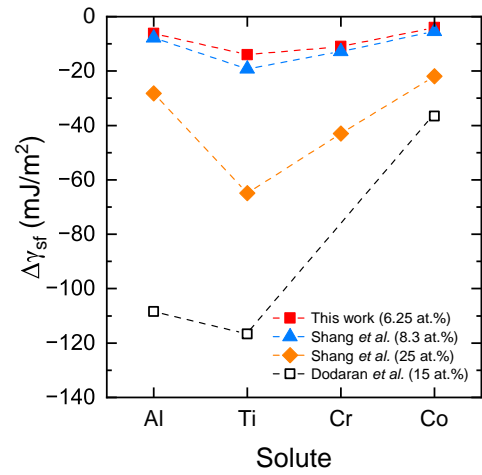


Figure A1. Variation of stacking faults energies with solutes for four different planar solute concentrations (in parentheses). The available literature data are taken from Refs. [45, 46, 68].

- [1] R. C. Reed, *The Superalloys Fundamentals and Applications* (Cambridge University Press, 2006).
- [2] R. Royce, *The jet engine* (John Wiley & Sons, 2015).
- [3] T. Pollock and S. Tin, *Journal of Propulsion and Power* **22**, 361 (2006).
- [4] P. Caron and T. Khan, *Aerospace Science and Technology* **3**, 513 (1999).
- [5] T. M. Pollock and S. Tin, *Journal of Propulsion and Power* **22**, 361 (2006).
- [6] H. Karnthaler, E. Mühlbacher, and C. Rentenberger, *Acta Materialia* **44**, 547 (1996).
- [7] Y. Umakoshi, D. Pope, and V. Vitek, *Acta Metallurgica* **32**, 449 (1984).
- [8] S.-L. Shang, J. Shimanek, S. Qin, Y. Wang, A. M. Beese, and Z.-K. Liu, *Phys. Rev. B* **101**, 024102 (2020).
- [9] G. Schoeck, S. Kohlhammer, and M. Fahnle, *Philosophical Magazine Letters* **79**, 849 (1999).
- [10] Y. M. Wang-Koh, *Materials Science and Technology* **33**, 934 (2017).
- [11] Y. Abate, S. Gamage, L. Zhen, S. Cronin, H. Wang,

- V. Babicheva, M. H. Javani, and M. Stockman, *Light: Science & Applications* **5**, 16162 (2015).
- [12] V. Paidar, D. Pope, and V. Vitek, *Acta Metallurgica* **32**, 435 (1984).
- [13] E. Chen, A. Tamm, T. Wang, M. E. Epler, M. Asta, and T. Frolov, *npj Computational Materials* **8**, 80 (2022).
- [14] G. Tichy, V. Vitek, and D. P. Pope, *Philosophical Magazine A* **53**, 467 (1986).
- [15] C. Rae and R. Reed, *Acta Materialia* **55**, 1067 (2007).
- [16] N. Matan, D. Cox, P. Carter, M. Rist, C. Rae, and R. Reed, *Acta Materialia* **47**, 1549 (1999).
- [17] B. H. Kear, J. M. Oblak, and A. F. Giamei, *Metallurgical Transactions* **1**, 2477 (1970).
- [18] G. R. Leverant, B. H. Kear, and J. M. Oblak, *Metallurgical Transactions* **4**, 355 (1973).
- [19] D. Knowles and Q. Chen, *Materials Science and Engineering: A* **340**, 88 (2003).
- [20] A. Breidi, J. Allen, and A. Mottura, *Acta Materialia* **145**, 97 (2018).
- [21] C. Rae, N. Matan, and R. Reed, *Materials Science and Engineering: A* **300**, 125 (2001).
- [22] L. Kovarik, R. Unocic, J. Li, P. Sarosi, C. Shen, Y. Wang, and M. Mills, *Progress in Materials Science* **54**, 839 (2009).
- [23] G. Viswanathan, P. Sarosi, M. Henry, D. Whitis, W. Milligan, and M. Mills, *Acta Materialia* **53**, 3041 (2005).
- [24] O. Mryasov, Y. Gornostyrev, M. van Schilfgaarde, and A. Freeman, *Acta Materialia* **50**, 4545 (2002).
- [25] Y. Qi and R. K. Mishra, *Phys. Rev. B* **75**, 224105 (2007).
- [26] L. Vitos, J.-O. Nilsson, and B. Johansson, *Acta Materialia* **54**, 3821 (2006).
- [27] C. B. Carter and S. M. Holmes, *The Philosophical Magazine: A Journal of Theoretical Experimental and Applied Physics* **35**, 1161 (1977).
- [28] M. F. de Campos, in *Advanced Powder Technology VI*, Materials Science Forum, Vol. 591 (Trans Tech Publications Ltd, 2008) pp. 708–711.
- [29] S. Ma, L. Carroll, and T. Pollock, *Acta Materialia* **55**, 5802 (2007).
- [30] P. C. J. Gallagher, *Metallurgical Transactions* **1**, 2429 (1970).
- [31] X. Xie, G. Chen, P. McHugh, and J. Tien, *Scripta Metallurgica* **16**, 483 (1982).
- [32] R. Li, L. Xie, W. Y. Wang, P. K. Liaw, and Y. Zhang, *Frontiers in Materials* **7** (2020), 10.3389/fmats.2020.00290.
- [33] Y. Ikeda, B. Grabowski, and F. Körmann, *Materials Characterization* **147**, 464 (2019).
- [34] S. Curtarolo, G. L. W. Hart, M. B. Nardelli, N. Mingo, S. Sanvito, and O. Levy, *Nature Materials* **12**, 191 (2013).
- [35] G. L. W. Hart, T. Mueller, C. Toher, and S. Curtarolo, *Nature Reviews Materials* **6**, 730 (2021).
- [36] V. Vitek, *The Philosophical Magazine: A Journal of Theoretical Experimental and Applied Physics* **18**, 773 (1968).
- [37] L. Li, T. Ungár, Y. Wang, J. Morris, G. Tichy, J. Lendvai, Y. Yang, Y. Ren, H. Choo, and P. Liaw, *Acta Materialia* **57**, 4988 (2009).
- [38] D. Pierce, J. Jiménez, J. Bentley, D. Raabe, and J. Wittig, *Acta Materialia* **100**, 178 (2015).
- [39] E. Tadmor and N. Bernstein, *Journal of the Mechanics and Physics of Solids* **52**, 2507 (2004).
- [40] J. Cahoon, Q. Li, and N. Richards, *Materials Science and Engineering: A* **526**, 56 (2009).
- [41] V. S. Sarma, J. Wang, W. Jian, A. Kauffmann, H. Conrad, J. Freudenberger, and Y. Zhu, *Materials Science and Engineering: A* **527**, 7624 (2010).
- [42] M. Chandran and S. K. Sondhi, *Journal of Applied Physics* **109**, 103525 (2011).
- [43] F. A. Mohamed and T. G. Langdon, *Acta Metallurgica* **22**, 779 (1974).
- [44] A. Argon and W. Moffatt, *Acta Metallurgica* **29**, 293 (1981).
- [45] X.-X. Yu and C.-Y. Wang, *Acta Materialia* **57**, 5914 (2009).
- [46] S. Shang, C. Zacherl, H. Fang, Y. Wang, Y. Du, and Z. Liu, *Journal of Physics: Condensed Matter* **24**, 505403 (2012).
- [47] S. Shang, W. Wang, Y. Wang, Y. Du, J. Zhang, A. Patel, and Z. Liu, *Journal of Physics: Condensed Matter* **24**, 155402 (2012).
- [48] D. J. Siegel, *Applied Physics Letters* **87**, 121901 (2005).
- [49] X.-X. Yu and C.-Y. Wang, *Materials Science and Engineering: A* **539**, 38 (2012).
- [50] N. Eurich and P. Bristowe, *Scripta Materialia* **102**, 87 (2015).
- [51] W. Yang, P. Qu, J. Sun, Q. Yue, H. Su, J. Zhang, and L. Liu, *Vacuum* **181**, 109682 (2020).
- [52] C. Hu, Z. Zhang, H. Chen, J. He, and H. Guo, *Journal of Alloys and Compounds* **843**, 155799 (2020).
- [53] F. Xia, W. Xu, Z. Shi, W. Xie, and L. Chen, *Mechanics of Materials* **165**, 104183 (2022).
- [54] X. Zhao, Y. Wang, X. Song, Y. Wang, and Z. Chen, *Computational Materials Science* **202**, 110990 (2022).
- [55] G. Kresse and J. Furthmüller, *Computational Materials Science* **6**, 15 (1996).
- [56] G. Kresse and J. Furthmüller, *Phys. Rev. B* **54**, 11169 (1996).
- [57] J. P. Perdew, K. Burke, and M. Ernzerhof, *Phys. Rev. Lett.* **77**, 3865 (1996).
- [58] M. Methfessel and A. Paxton, *Phys. Rev. B* **40**, 3616 (1989).
- [59] P. E. Blöchl, O. Jepsen, and O. K. Andersen, *Phys. Rev. B* **49**, 16223 (1994).
- [60] A. Datta, U. Waghmare, and U. Ramamurty, *Scripta Materialia* **60**, 124 (2009).
- [61] J. Han, X. Su, Z.-H. Jin, and Y. Zhu, *Scripta Materialia* **64**, 693 (2011).
- [62] S. Ogata, J. Li, and S. Yip, *Science* **298**, 807 (2002).
- [63] M. Jahnátek, J. Hafner, and M. Krajčí, *Phys. Rev. B* **79**, 224103 (2009).
- [64] A. V. Ruban and H. L. Skriver, *Phys. Rev. B* **55**, 856 (1997).
- [65] C. Jiang and B. Gleeson, *Scripta Materialia* **55**, 433 (2006).
- [66] Q. Wu and S. Li, *Computational Materials Science* **53**, 436 (2012).
- [67] J. R. Rice, *Journal of the Mechanics and Physics of Solids* **40**, 239 (1992).
- [68] M. S. Dodaran, S. Guo, M. M. Khonsari, N. Shamsaei, and S. Shao, *Computational Materials Science* **191**, 110326 (2021).
- [69] K. Badura-Gergen and H.-E. Schaefer, *Phys. Rev. B* **56**, 3032 (1997).
- [70] M. H. F. Sluiter and Y. Kawazoe, *Phys. Rev. B* **51**, 4062 (1995).
- [71] S. Liu, M. Wen, Z. Li, W. Liu, P. Yan, and C. Wang, *Materials & Design* **130**, 157 (2017).
- [72] H. Zhu, J. Wang, L. Wang, Y. Shi, M. Liu, J. Li, Y. Chen, Y. Ma, P. Liu, and X.-Q. Chen, *Journal of Materials Science & Technology* **143**, 54 (2023).
- [73] S. B. Maisel, M. Höfler, and S. Müller, *Phys. Rev. B* **94**, 014116 (2016).
- [74] C. Booth-Morrison, Z. Mao, R. D. Noebe, and D. N. Seidman, *Applied Physics Letters* **93**, 033103 (2008).
- [75] B. Wei, Y. Lin, Z. Huang, L. Huang, K. Zhou, L. Zhang, and L. Zhang, *Acta Materialia* **240**, 118336 (2022).
- [76] S. Walston, A. Cetel, R. MacKay, K. OHara, D. Duhl, and R. Dreshfield, in *Superalloys 2004* (2005).
- [77] J. Zhang, T. Murakumo, Y. Koizumi, T. Kobayashi, and H. Harada, *Acta Materialia* **51**, 5073 (2003).
- [78] T. Kobayashi, H. Harada, M. Osawa, and A. Sato, *Journal of*

- The Japan Institute of Metals **69**, 1099 (2005).
- [79] T. Yokokawa, H. Harada, K. Kawagishi, T. Kobayashi, M. Yuyama, and Y. Takata, in *Superalloys 2020*, edited by S. Tin, M. Hardy, J. Clews, J. Cormier, Q. Feng, J. Marcin, C. O'Brien, and A. Suzuki (Springer International Publishing, Cham, 2020) pp. 122–130.
- [80] K. Kawagishi, A.-C. Yeh, T. Yokokawa, T. Kobayashi, Y. Koizumi, and H. Harada, “Development of an oxidation-resistant high-strength sixth-generation single-crystal superalloy tms-238,” in *Superalloys 2012* (John Wiley & Sons, Ltd, 2012) pp. 189–195.
- [81] S. Cao, Y. Yang, B. Chen, K. Liu, Y. Ma, L. Ding, and J. Shi, *Journal of Materials Science & Technology* **86**, 260 (2021).